Materials Advances

ROYAL SOCIETY OF CHEMISTRY

PAPER

View Article Online
View Journal

Cite this: DOI: 10.1039/d5ma01417d

Biocompatible melanin-functionalized $CaCO_3$ nanoparticles for cell protection against photoinduced oxidative stress

Giuseppe Vitiello, *[ab] Francesca Baldassarre,[c] Chiara Boncristiani, [de] Alessandro Pezzella, [fg] Giuseppina Luciani,[a] Giuseppe Ciccarella [cd] and Viviana Vergaro *[e]

Melanin is a natural biopolymer with intrinsic antioxidant, photoprotective, and anti-inflammatory properties, making it a promising component for bioinspired functional materials. In this study, we report a green, one-pot synthesis of hybrid melanin–calcium carbonate nanoparticles (melanin–$CaCO_3$ NPs) *via in situ* polymerization of 5,6-dihydroxyindole-2-carboxylic acid (DHICA) on amino-functionalized $CaCO_3$ templates. The resulting nanoparticles combine the biocompatibility of the inorganic scaffold with the multifunctionality of melanin. Detailed physicochemical characterization confirmed the successful formation of the hybrid system, while *in vitro* studies on two human cell lines demonstrated excellent cytocompatibility, promotion of cell proliferation, and marked reactive oxygen species (ROS)-scavenging ability, achieving approximately 70% ROS reduction at a dose of 10 μg mL^{-1}. Notably, even with a low melanin content (1%), the NPs exhibited significant intracellular photoprotective activity against photoinduced oxidative stress. These findings suggest that melanin–$CaCO_3$ NPs hold strong potential as green-engineered, multifunctional nanomaterials for biomedical applications, particularly in oxidative stress-related therapies and photoprotection.

Received 5th December 2025,
Accepted 23rd March 2026

DOI: 10.1039/d5ma01417d

rsc.li/materials-advances

1. Introduction

Oxidative stress (OS) is a critical contributor to the onset and progression of numerous pathological states, as it is closely linked to a wide range of cellular and tissue injuries that adversely affect various organs and biological systems.[1–3] OS is caused by the imbalance between the generation and clearance of oxidant species, which are mainly composed of reactive oxygen species (ROS).[4–6] These species are generated through a combination of endogenous mechanisms – such as the activity of fibroblasts, epithelial and endothelial cells, immune cells, mitochondrial respiration, and NADPH oxidase – and exogenous influences, including exposure to environmental pollutants, radiation, toxic compounds, and certain pharmaceuticals. Prolonged exposure to UVA radiation is especially detrimental, as it enhances the intracellular buildup of ROS, exacerbates oxidative stress, and triggers molecular damage—manifesting in lipid peroxidation, alterations of the protein structure, and genomic instability within skin cells. These can significantly contribute to accelerated photoaging, weakened immune response to UV exposure, and the development of UV-related skin tumors.[7,8] Under normal physiological conditions, human cells exploit their enzymatic and non-enzymatic antioxidant defence systems for maintaining the cellular redox balance.[9] In the presence of inefficient and insufficient defence systems, the oxidant species can accumulate favouring serious pathological conditions such as diseases, disorders and aging with a progressive loss of function in tissues and organs.[1]

In recent years, considerable research has focused on the creation of biocompatible nanomaterials that emulate natural systems and exhibit strong radical-scavenging capabilities.[10–12] These materials play a key role in modulating the redox balance by neutralizing oxidant species and sustaining antioxidant defences, thereby contributing to cellular protection under

[a] Department of Chemical, Materials and Production Engineering, University of Naples Federico II, p.le V. Tecchio 80, 80125 Naples, Italy. E-mail: giuseppe.vitiello@unina.it
[b] Center for Colloid and Surface Science, CSGI, Via della Lastruccia 3, Florence, 50019, Italy
[c] Biological and Environmental Sciences Department, UdR INSTM of Lecce University of Salento, Via Monteroni, 73100 Lecce, Italy
[d] Institute of Nanotechnology CNR NANOTEC, Consiglio Nazionale delle Ricerche, Via Monteroni, 73100 Lecce, Italy
[e] Department of Experimental Medicine, University of Salento, Via Monteroni, 73100 Lecce, Italy. E-mail: viviana.vergaro@unisalento.it
[f] Department of Physics "Ettore Pancini", University of Naples Federico II, Via Cintia 4, 80126 Naples, Italy
[g] Institute of Polymers, Composites and Biomaterials, National Research Council, 80125 Naples, Italy

physiological conditions. Current strategies have further evolved from simple radical scavenging to the engineering of intelligent 'synthetic organelles' capable of autoregulatory protection. For instance, recent work has demonstrated the potential of enzyme-loaded nanoreactors that not only scavenge ROS directly but also trigger endogenous glutathione biosynthesis in response to oxidative stress, ensuring durable maintenance of intracellular redox homeostasis.[13] Consequently, there is increasing interest in the design and development of bio- and eco-compatible nanotechnological formulations aimed at protecting the skin and other tissues from the harmful effects of UV radiation. This includes the advancement of sunscreens and antioxidant-enriched skincare products with improved stability, effectiveness, and targeted delivery.[14,15] In this context, melanin-like materials are considered highly promising candidates for these aims. They are polyphenolic-like pigments found in many different natural sources, from bacteria, fungi and plants to fish, mollusks, mammals, and humans, which are involved in a variety of biological functions and shield organisms from harmful environmental factors.[16] Notably, melanins contribute significantly to physiological balance, especially by regulating functions in the skin, hair, and eyes and by offering protection against stress-related genetic damage.[17,18] Due to their notable physicochemical properties—such as biocompatibility, ability to scavenge reactive oxygen and nitrogen species (RONS), broad-spectrum light absorption spanning UV and visible ranges, high photostability, heat conversion efficiency, electrical conductivity, and paramagnetism[19]—melanins are promising macromolecules for developing functional biomaterials aimed at skin protection,[20] wound repair,[21,22] and eco-friendly antioxidant, antibacterial,[23,24] or photoresponsive biomedical applications.[25] Interestingly, melanin precursors, such as 5,6-dihydroxyindole (DHI), 5,6-dihydroxyindole-2-carboxylic acid (DHICA), and dopamine (DA), have been successfully integrated at the molecular level with ceramic components – including titanium,[26] silica,[27] and cerium[28] oxides, as well as doped hydroxyapatite[29] – resulting in hybrid nanoplatforms that exhibit strong antimicrobial and antioxidant activities, along with notable bioactive and diagnostic properties. Recent advances in the design and tuning of such hybrid nanostructures, including core–shell and cloud-type morphologies, are discussed in detail in the work by Pota *et al.*,[30] which explores how structural modifications can optimize functional properties for biomedical applications. Despite the significant progress in melanin–hybrid nanostructures, many existing systems remain constrained by the use of persistent, non-biodegradable inorganic cores, such as silica or metal oxides, which pose long-term biosafety concerns regarding tissue accumulation. Furthermore, most reported melanin–$CaCO_3$ architectures rely on the physical adsorption of the pre-formed pigment or multi-step coating procedures that often result in limited interfacial stability and low radical-scavenging efficiency. There is a clear need for simpler, 'green' synthetic routes that can achieve a high degree of integration between the biopolymer and the inorganic scaffold. By leveraging the *in situ* oxidative polymerization of DHICA directly on $CaCO_3$ templates, we overcome these hurdles, producing a highly stable, biomimetic hybrid that ensures maximum synergy between the mineral phase and the melanin network while maintaining full biodegradability. Beyond traditional ceramic hybrids, a variety of other nanostructures have been extensively explored for photoinduced ROS scavenging and photoprotective applications, demonstrating the diversity of the field. For instance, recent studies have highlighted the efficacy of specific polymer-based and metal-doped nanoparticles in mitigating oxidative stress under irradiation.[31–33] However, despite the progress in these systems, $CaCO_3$ stands out as a particularly compelling platform due to its unique combination of extreme biocompatibility, pH-dependent biodegradability, and high loading capacity for bioactive macromolecules. Naturally abundant and found in structures like mollusk shells, $CaCO_3$ offers a safe and sustainable 'green chemistry' route that avoids the potential long-term accumulation or toxicity issues sometimes associated with synthetic metal-oxide or polymeric scaffolds.

Calcium carbonate ($CaCO_3$), a naturally occurring inorganic material, is valued in biomedical contexts for its biocompatibility and ability to biodegrade safely. In diverse biomedical applications, $CaCO_3$ shows significant potential, especially in drug delivery, tissue regeneration, and imaging techniques. $CaCO_3$ nanoparticles can serve as adjuvants in vaccine formulations, helping to boost the immune response. Current studies aim to enhance the properties of these materials and broaden their applications to achieve better therapeutic results. In recent years, $CaCO_3$ nanoparticles have been widely utilized in combination with imaging contrast agents and therapeutic compounds for diverse diagnostic and therapeutic applications.[34] Naturally abundant, calcium carbonate is a major component of materials, such as mollusk shells, limestone, or eggshells, and is highly intriguing for driving advancements in novel biomedical systems in accordance with the safe and sustainable nanotechnology design principle. Further advantages include ease of preparation using gentle methods such as co-precipitation and their ability to biodegrade into harmless by-products at neutral pH, preventing the accumulation of these materials in the body over time.[35] Furthermore, due to $CaCO_3$'s strong ability to capture bioactive molecules, it has been extensively utilized in biomedical research as a sacrificial template for creating functional materials to explore cellular vesicle acidification or enzyme compartmentalization effects in catalytic cascades.[36,37] Through the use of $CaCO_3$ nanoparticles combined with drugs, a variety of treatments such as chemical therapy, gene therapy, photothermal therapy (PTT)/photodynamic therapy (PDT), and immunotherapy can be accomplished.[38] One of the unique features of these inorganic nanomaterials is that their intrinsic physical, chemical and biological properties can be easily tuned and enhanced by surface functionalization. By exploiting their surface functionalization, multifunctional nanosystems can easily achieve (i) modification of their original surface chemical termination, (ii) incorporation of new functional molecules onto the surface, or (iii) coating of the surface with an additional layer.[34] This study focused on designing and synthesizing

melanin-functionalized calcium carbonate nanoparticles (melanin–$CaCO_3$ NPs) endowed with enhanced protective capabilities against oxidative stress, including that induced by light exposure. A feasible synthetic strategy was proposed to realize bio-functional nanostructures, in which crystalline nano-calcium carbonate platforms were combined with DHICA monomers to induce the oxidative polymerization to melanin. The formation, chemical composition, and structural properties of the hybrid nanoparticles were thoroughly characterized, along with evaluations of their biocompatibility, antioxidant activity, and reactive oxygen species (ROS) scavenging under light exposure, indicating strong prospects for biomedical uses.

2. Materials and methods

2.1 Materials

EDC (protein seq grade), NHS (98%), APTES (99.999%), ethanol (absolute, ≥99.8%), fluorescein isothiocyanate (FITC), 3-(4,5-dimethylthiazol-2-yl)-2,5-diphenyl-tetrazolium bromide (MTT), Hoechst 33342 (trihydrochloride and trihydrate), phosphate buffer saline (PBS) and Annexin V were purchased from Sigma-Aldrich and used as received. H_2DCFDA was purchased from Thermo Fisher Scientific and used as received. The DHICA monomer and DHICA–melanin were prepared as described elsewhere.[39]

2.2 Synthesis of melanin–$CaCO_3$ nanoparticles

$CaCO_3$ nanocrystals ($CaCO_3$-NCs) were prepared through a spray drying process as described in our previous work.[35] Briefly, in spray drying, $CaCl_2$ solution and $NaHCO_3$ are mixed under controlled conditions, because the concentration of the precursor solutions ensures the optimal precipitation and nanocrystal formation. The pH of the solution is also crucial, as it can affect the size and morphology of the obtained $CaCO_3$ crystals. Thanks to the high temperature, the liquid feed is atomized into fine droplets, which are then rapidly dried in a hot air stream. This process results in the formation of solid particles with a desired size distribution and morphology.

Then, the surface of the obtained $CaCO_3$ nanocrystals was functionalized with 3-aminopropyl-triethoxysilane (APTES), as previously described in the literature.[40,41] In particular, a mixture of APTES (1.0 M) and $CaCO_3$-NCs (0.150 g) in toluene was prepared and the reaction was allowed to proceed at 90 °C for 18 h in the dark under continuous stirring. Then, the amino-functionalized $CaCO_3$ nanocrystals (named NH_2-$CaCO_3$-NCs) were recovered by centrifugation at 3500 rpm for 5 minutes, washed three times with distilled water and dried at 100 °C for 24 h. The NH_2-$CaCO_3$-NC weight was then calculated to obtain the NH_2-$CaCO_3$-NC : DHICA molar ratio of 2 : 1 in the reaction mixture. The DHICA/NH_2-$CaCO_3$-NC precursor was synthesized by coupling DHICA carboxyl (–COOH) groups to amino groups of APTES molecules through EDC/NHS chemistry. EDC (0.021 mM), NHS (0.25 mM), and NH_2-$CaCO_3$-NCs (6.0 mg) were added to a DHICA deaerated solution (0.4 mM) in ethanol (43.2 mL) and water (9.00 mL). The reaction was allowed to proceed under stirring for 15 min at 4 °C in an ice bath. The pH of solution was measured (pH 10.5) to verify the alkalinity of experimental conditions. Alkaline experimental conditions facilitate the polymerization of melanin by promoting the oxidation of DHICA precursors, improving the interaction between melanin and inorganic nanoparticles, enhancing melanin's stability and structure, and enabling better control over the functionalization of nanoparticles. The NPs were recovered by centrifugation and repeatedly washed (5 times with distilled water).

Fluorescent melanin–$CaCO_3$ nanoparticles (melanin–$CaCO_3$ NPs) were prepared by incubating NH_2-$CaCO_3$ nanocrystals (20 mg) with fluorescent isothiocyanate (0.4 mM) in an ethanol/water solution. The reaction was allowed to proceed for 6 h in the dark under continuous stirring. The chemical conjugation between $CaCO_3$-NH_2 and fluorescein isothiocyanate (FITC) typically involves a reaction between the amino group on the $CaCO_3$-NH_2 surface and the isothiocyanate group (–N═C═S) of the FITC molecule. FITC is an isothiocyanate derivative, which contains a reactive –N═C═S group. The primary amino group (NH_2) on the surface of the $CaCO_3$ particles can undergo a nucleophilic attack on the carbon atom of the isothiocyanate group of FITC. This reaction leads to the formation of a stable thiourea bond (–NH–C(S)–N–) between the $CaCO_3$-NH_2 surface and FITC. The reaction is often carried out under mildly alkaline conditions (pH 8–9), which promotes the deprotonation of the amino group (NH_2), enhancing its nucleophilicity and thus improving the conjugation efficiency.[42]

2.3 Physicochemical characterization

2.3.1 Transmission electron microscopy (TEM). The TEM images were captured using a JEOL JEM 1400Plus microscope, which is equipped with a Gatan Orius SC600 bottom-view camera and a LaB6 filament. The microscope operated at an accelerating voltage of 80 kV to minimize potential damage to the organic coating. Sample preparation involved dispersing the obtained powders in an aqueous solution, followed by depositing a drop of this suspension onto one side of transparent, polymer-coated 200 mesh copper grids. The nanoparticle size distribution was determined by analyzing at least ten different regions on the TEM grid using ImageJ software. Measurements were performed using the oval selection tool, calibrated against the scale bar embedded in each TEM image. Particle diameters were computed under the assumption that the nanoparticles are spherical.

2.3.2 Dynamic light scattering (DLS). The hydrodynamic diameter and zeta potential of the nanoparticles were determined using a Malvern Zetasizer Nano ZS *via* dynamic light scattering (DLS) analysis. All measurements were performed at 25 °C. To prepare the samples, a small volume of the original suspension was diluted with ultrapure water (ddH_2O) using a syringe pre-filled with water. The diluted samples were then introduced into a disposable zeta potential cell, ensuring the exclusion of air bubbles prior to placing the cell into the instrument for analysis. Particle zeta potential was measured using laser Doppler velocimetry (LDV). The reported ζ-potential

values are the average of five independent measurements, each consisting of five runs, to ensure reliability and repeatability.

2.3.3 UV-Vis absorption and emission spectra. Optical characterization was carried out by recording UV-vis absorption and emission spectra using a Varian Cary 500 spectrophotometer and a Varian Cary Eclipse spectrofluorometer, respectively. All spectral data were obtained in deionized (DI) water. For all measurements, quartz cuvettes with a 1 cm path length were employed.

2.3.4 Electron paramagnetic resonance (EPR) spectroscopy. EPR measurements were conducted utilizing a Bruker Elexsys E-500 spectrometer operating at X-band (9 GHz) frequency, equipped with an ultrasensitive probe head (Rheinstetten, Germany). A precisely weighed amount (2 mg) of each powdered sample was loaded into a quartz tube, which was then inserted coaxially into a standard 8 mm quartz EPR sample tube for spectral acquisition at a temperature of 25 ± 2 °C. Instrumental parameters were set in accordance with established protocols,[43] including a sweep width of 100 G, a resolution of 1024 points, and a modulation frequency and amplitude of 100 kHz and 1.0 G, respectively. Spectra were acquired with an attenuation of 20 dB, and 128 scans were accumulated to improve the signal-to-noise ratio. To facilitate accurate determination of the *g*-factor and spin-density, an internal standard consisting of Mg^{2+}/MnO powder was placed coaxially within the same quartz tube alongside the samples. Then, power saturation (PS) curves were also recorded by varying the microwave power from 0.004 mW to 128 mW. Quantitative analysis involved measuring the line width (ΔB), defined as the peak-to-peak separation of the first-derivative spectral signal, which reflects the instrument's response. All measurements were performed in triplicate using independently prepared samples for each system, allowing estimation of experimental variability. The resulting uncertainty was approximately 30% for the radical concentration and $\pm 2 \times 10^{-4}$ for the *g*-factor.

2.3.5 Thermogravimetric analysis (TGA). TGA was carried out using a TA Instrument thermoanalyser SDT Q600 (TA Instrument, New Castle, DE, USA) to study the thermal behavior of obtained samples. Approximately 2 mg of each sample was tested under a nitrogen atmosphere at a heating rate of 10 °C min^{-1}.

2.3.6 Fourier transform infrared spectroscopy using attenuated total reflection (FTIR/ATR). Fourier transform infrared spectroscopy using attenuated total reflection (FTIR/ATR) analysis was performed by using a Nexus FT-IR spectrometer and positioning the samples on a crystal of ZnSe. The FTIR absorption spectra were recorded in the 4000–400 cm^{-1} range with a spectral resolution of 8 cm^{-1}.

2.4 Biological investigation

2.4.1 Cell culture. As shown previously in ref. 44, the human fibroblast cell line WS1 (ATCC®CRL-1502™) (RRID: CVCL_0560) was procured from ATCC (Manassas, VA), whereas human immortalized keratinocytes (HaCaT) (RRID: CVCL_0038) were obtained from Innoprot (Derio, Spain). The cells were cultured in Dulbecco's modified Eagle medium (DMEM) supplemented with 10% fetal bovine serum, 2 mM L-glutamine, and antibiotics. They were maintained in a humidified incubator with 5% CO_2 at 37 °C. Cultures were passaged every 48 hours at a 1 : 5 dilution. Prior to passaging, the culture medium was aspirated, the cells were rinsed with phosphate-buffered saline (PBS) and then detached with trypsin–EDTA. Following centrifugation at 1200 rpm for five minutes, the resulting cell pellet was resuspended in fresh culture medium.

2.4.2 Analysis of cell viability. As previously demonstrated in ref. 45, cells were seeded into 96-well plates at a volume of 100 μL per well, achieving a cell density of 2.5×10^3 cells per cm^2. Following a 24 hour incubation period post-seeding, the cells were exposed to increasing concentrations (ranging from 1 to 200 μg mL^{-1}) of $CaCO_3$-NC, NH_2-$CaCO_3$-NCs, and melanin–$CaCO_3$ nanoparticles. Stock suspensions of these nanoparticles were prepared in distilled water at a concentration of 0.2 mg mL^{-1}, and appropriate aliquots were added to the culture medium to attain the desired final concentrations. After 24 hours of treatment, cell viability was evaluated using the MTT assay. Additional assessments were performed at 24, 48, and 72 hours by treating both cell lines with 100 μg mL^{-1} of each nanoparticle formulation. For the assay, the MTT reagent dissolved in DMEM without phenol red was added at a concentration of 0.5 mg mL^{-1}. Following a 3 hour incubation at 37 °C, the medium containing MTT was removed, and the resulting formazan crystals were dissolved in 100 μL of DMSO per well. The absorbance of the blue formazan was measured at 570 nm using an automated plate reader (Microbeta Wallac 1420, PerkinElmer, Milan, Italy). Cell viability was expressed as the percentage of surviving cells relative to control groups, which included untreated cells and cells treated with equivalent volumes of DMSO to account for any effects of the solvent on cell viability.

2.5 Cell proliferation

As has been previously demonstrated in ref. 45, cell proliferation was evaluated in human fibroblasts (WS1) and human keratinocytes (HaCaT) using the Hoechst assay, which enables quantification of cellular DNA.[46] Briefly, cells were incubated for 24 hours with 100 μg mL^{-1} of $CaCO_3$ nanocrystals ($CaCO_3$-NCs), as well as 100 μg mL^{-1} of NH_2-functionalized $CaCO_3$ nanocrystals (NH_2-$CaCO_3$-NCs) and melanin-coated $CaCO_3$ nanoparticles (melanin–$CaCO_3$ NPs). Following incubation, the cells were harvested from 12-well plates and suspended in 100 μL of Hoechst buffer (composed of 0.1 M NaCl, 1 mM EDTA, and 10 mM Tris, pH 7.4). To facilitate cell lysis and DNA release, the suspensions were subjected to five cycles of freezing and thawing. The assay was performed in black, fat-bottom plates with low background fluorescence to enhance detection sensitivity. Fluorescence measurements were obtained using a PerkinElmer LS50 spectrofluorometer (excitation at 360 nm and emission at 460 nm). A calibration curve was prepared using calf thymus DNA standards to quantify the DNA concentration. Each sample's DNA content, expressed in micrograms per milliliter (μg mL^{-1}), was determined by comparing its

fluorescence intensity to the standard curve, following the addition of 2 μL of Hoechst dye to each sample.

2.5.1 UVA irradiation and H_2DCFDA assay. To assess the protective efficacy of melanin–$CaCO_3$ nanoparticles (NPs) against oxidative stress, cells were seeded at a density of 3.5×10^4 cells per cm^2 in 60 mm eukaryotic cell culture plates, as shown previously in ref. 44. The cells were pre-treated with increasing concentrations of melanin–$CaCO_3$ NPs (ranging from 0.1 to 10 μg mL^{-1}) for 120 minutes prior to exposure. Oxidative stress was induced by UVA irradiation at 100 J cm^{-2} for 10 minutes. Following irradiation, cells were incubated with the cell-permeable, redox-sensitive dye H_2DCFDA at a final concentration of 20 μM for 30 minutes at 37 °C. Subsequently, cells were washed twice with cold PBS, detached using trypsin, centrifuged at 1000 rpm for 10 minutes, and resuspended in PBS supplemented with 30 mM glucose, 1 mM $CaCl_2$, and 0.5 mM $MgCl_2$ (referred to as PBS plus) to achieve a cell density of 1×10^5 cells per mL. H_2DCFDA remains non-fluorescent until hydrolyzed by intracellular esterases; in the presence of reactive oxygen species (ROS), it is oxidized to the highly fluorescent 2′,7′-dichlorofluorescein (DCF). Fluorescence intensity of DCF was measured at an emission wavelength of 525 nm, with excitation set at 488 nm, using a PerkinElmer LS50 spectrofluorometer (PerkinElmer, Milan, Italy). Spectral data were acquired at a scanning speed of 300 nm min^{-1}, with a slit width of 5 nm for both excitation and emission. ROS production was quantified and expressed as a percentage relative to the fluorescence intensity of untreated control samples. Additional controls included $CaCO_3$-NC and NH_2-$CaCO_3$-NC nanoparticles.

2.5.2 Quantification of the internalized melanin-based NPs. HaCaT and WS1 cells were seeded at a density of 3.5×10^4 cells per cm^2 on 100 mm diameter eukaryotic cell culture plates and incubated in complete medium for 24 hours. Subsequently, the cells were exposed to 10 μg mL^{-1} of melanin–$CaCO_3$ nanoparticles for 60 minutes. Following treatment, total cell lysates were prepared by resuspending each cell pellet in 50 μL of lysis buffer composed of 100 mM Tris–HCl, 300 mM NaCl, and 0.5% NP-40 at pH 7.4, supplemented with protease and phosphatase inhibitors. Protein concentrations were determined using the Bradford assay, and 50 μg of protein extracts were diluted in 1 mL of 50 mM potassium phosphate buffer (pH 7.0). UV-visible spectra were recorded to analyze the samples. The extent of melanin–$CaCO_3$ nanoparticle internalization by the cells was quantified by referencing a calibration curve established with known concentrations of melanin–$CaCO_3$ nanoparticles alone. For this purpose, UV-vis spectra were obtained from samples containing increasing concentrations (1–100 μg mL^{-1}) of melanin–$CaCO_3$ nanoparticles, both in the absence and presence of 50 μg of cell lysate. The calibration curves were generated by plotting absorbance values at 320 nm against nanoparticle concentrations.[44]

2.5.3 Staining of living cells and confocal microscopy investigation. The procedure for staining living cells has been described in our previous publication.[47] Specifically, HaCaT and WS1 cells were cultured on 35 mm glass-bottom Petri dishes and allowed to grow in complete media for 24 hours. Subsequently, the cells were exposed to melanin–$CaCO_3$ nanoparticles at a concentration of 10 μg mL^{-1}, for either 30 minutes or 2 hours. These nanoparticles were conjugated with FITC. Following incubation, the cells were rinsed twice with phosphate-buffered saline (PBS), then stained with Hoechst dye, and immediately imaged using confocal microscopy, with complete media lacking phenol red. Imaging was performed using a Zeiss LSM700 confocal microscope (Zeiss, Germany) mounted on a Zeiss Axio Observer Z1 inverted microscope, equipped with a 63× oil immersion objective with a 1.46 numerical aperture. Fluorescence excitation was achieved with laser lines at 405 nm for Hoechst and 488 nm for FITC-conjugated nanoparticles.

2.6 Protective effect of melanin–$CaCO_3$ NPs by flow cytometry analysis

As reported in our previous work[48] to analyze the cytocompatibility and the protective effects of melanin–$CaCO_3$ NPs against the cytotoxic effect of hydrogen peroxide in apoptosis induction, both HaCaT and WS1 human cells were incubated for 24 h with the melanin–$CaCO_3$ NPs and, after washing out of the particles, were treated with 1 mM H_2O_2 for 30 min to induce cell death. After 24 h of stress induction, cells are extensively washed with PBS, gently collected using 1× PBS/2 mM EDTA and incubated with Annexin V (BD Biosciences) for 20 min at room temperature in the dark according to the manufacturer's instructions. Annexin V marks phosphatidylserine exposed on the outer leaflet of the plasma membrane of dying cells. $CaCO_3$-NCs and NH_2-$CaCO_3$-NCs were also tested as control. Apoptosis (percentage of cells positive for annexin V) was measured with a FACS flow cytometer Accuri C6 (Becton Dickinson).

3. Results and discussion

3.1 Chemical conjugation and physicochemical properties of melanin–$CaCO_3$ NPs

The experimental approach developed to obtain melanin–$CaCO_3$NPs is illustrated in Fig. 1. Melanin–$CaCO_3$ NPs were obtained through the oxidative polymerization of DHICA (0.4 mM) on $CaCO_3$ NPs functionalized with 3-aminopropyltrimethoxysilane (APTES). DHICA was selected as the melanin precursor due to its structural and electronic features. The presence of the carboxyl group affects both the polymerization pattern and the supramolecular organization, leading to eumelanin-like materials with distinct redox properties compared to DHI- or dopamine-derived melanins. This is particularly relevant for applications where controlled radical behavior and redox buffering capacity are required.

More in detail, the synthetic approach relied at first on the formation of amino-functionalized $CaCO_3$ NPs (6.0 mg)[36] and then, the conjugation of APTES–DHICA was obtained through the coupling reaction between the amino group of APTES and the carboxyl group of DHICA using the *N*-(3-(dimethylamino)-propyl)-*N*′-ethyl-carbodiimide hydrochloride (EDC)/*N*-hydroxy

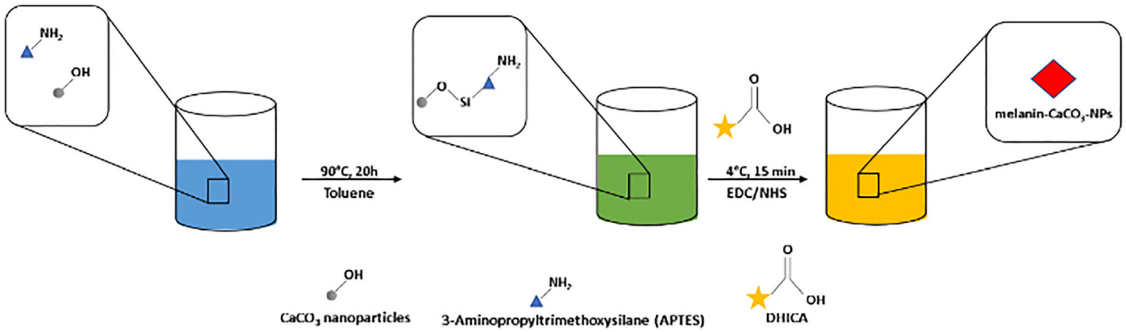

Fig. 1 Schematic view of design and preparation of $CaCO_3$–melanin nanoparticles.

succinimide (NHS) reaction. The reaction parameters were adapted from existing studies,[37] with a controlled low temperature to prevent unwanted side reactions.[38] The reaction yield was 90% based on weight measurement. The alkaline experimental condition is guaranteed by the presence of $CaCO_3$ alone. The pH plays a crucial role in the polymerization of DHICA to melanin on the inorganic nanoparticles: the functional groups on both the $CaCO_3$ nanocrystals and melanin molecules can interact more efficiently under alkaline conditions. The pH can influence the redox reactions occurring in the precursor molecule; in fact, DHICA undergoes oxidation and polymerization under alkaline conditions. The hydroxyl groups on the precursor molecules are deprotonated at high pH, promoting the nucleophilic attack on the substrates and aiding the formation of reactive intermediates that drive melanin formation. Alkaline conditions stabilize certain intermediates and may facilitate better polymerization of melanin by enabling the aggregation of the oxidative products that eventually form the melanin structure.

To produce FITC-labeled melanin–$CaCO_3$ nanoparticles, the amino-functionalized $CaCO_3$ particles were allowed to react with fluorescein isothiocyanate (FITC). NP characterization was assessed using both dynamic light scattering (DLS) measurements and TEM images. DLS measurements were assessed for each step of synthesis procedure as summarized in Table 1. Naked $CaCO_3$ nanocrystals in water tend to aggregate, as demonstrated by the higher hydrodynamic diameter and polydispersity index. The amino functionalization improves colloidal stability, as suggested by a lower PDI, and increases the surface charge to a positive value (+14.8 mV). Indeed, the oxidative polymerization of DHICA on amino-functionalized $CaCO_3$ nanoparticles led to a significant modification of the ζ-potential value (-17.4 ± 3.8 mV), and the size seems to be smaller (323 ± 5.0 nm) probably due to the minor aggregation phenomena that occur in water, as confirmed by both the single broad population (Fig. S1) and the low PDI (0.15). The morphological characterization of melanin–$CaCO_3$ NPs was conducted by TEM analysis, which revealed good sample preparation and dispersion of nanoparticles with an almost round-shaped nanostructures (Fig. S1 and Fig. 2a). According to the nanoparticle size distribution (Fig. 2b), almost 50% of analyzed nanoparticles show a dimension of about 104 ± 1 nm in diameter. This result compared to the DLS one confirmed the tendency of nanoparticles to self-aggregate in aqueous medium, leading to the formation of clusters of melanin–$CaCO_3$ NPs with a mean size greater than that of single one as observed by TEM. Furthermore, the DLS measurements were performed for 21 days to verify the stability of melanin–$CaCO_3$ synthetized NPs (Fig. S2). Fig. S2 indicates that DHICA functionalization enhances colloidal stability and reduces the tendency to aggregate, which are critical features for biomedical applications such as biodistribution and cellular uptake.

Table 1 Dynamic light scattering characterization of $CaCO_3$-based nanoparticles

Sample	Size (nm)	PDI (polydispersity index)	ζ-Potential (MV)
$CaCO_3$-NC	760.1 ± 1.6	0.426	-4.5 ± 1.23
NH_2-$CaCO_3$-NC	427.2 ± 3.5	0.313	$+14.8 \pm 0.70$
Melanin–$CaCO_3$ NPs	323 ± 5.0	0.15	-17.4 ± 3.8

EPR analysis was performed to evaluate the polymerization of DHICA into melanin and to explore the chemical and structural features of the pigment component within the melanin–$CaCO_3$ nanoparticles. As shown in Fig. 3A, the EPR spectrum of melanin–$CaCO_3$ NPs exhibited a single symmetric signal centered at a g-factor of 2.0037 ± 0.0003, with a linewidth (ΔB) of 6.8 ± 0.2. These parameters, derived from the experimental spectrum described in Fig. 3A, provided indirect insight into the chemical environment and spatial distribution of paramagnetic centers within the pigment matrix. This signal is characteristic of carbon-centered radicals typical of melanin and melanin-like pigments, as previously reported.[34,49,50] A similar EPR profile was observed for pure DHICA-derived melanin, showing a g-factor of 2.0035 ± 0.0003 and $\Delta B = 5.7 \pm 0.2$. The difference observed in the ΔB values confirms that the supramolecular organization of the melanin coating onto $CaCO_3$ nanoparticles is directly influenced by its interaction with the inorganic matrix, in contrast to pure melanin. This interpretation is further supported by the distinct trends observed in the power saturation curves, as illustrated in Fig. 3B, indicating that melanin supported on $CaCO_3$ exhibits a different microstructural organization, which may favour the exposure of redox-active sites, in agreement with previous evidence.[37] Complementary to the paramagnetic characterization, the optical properties were investigated by UV-vis

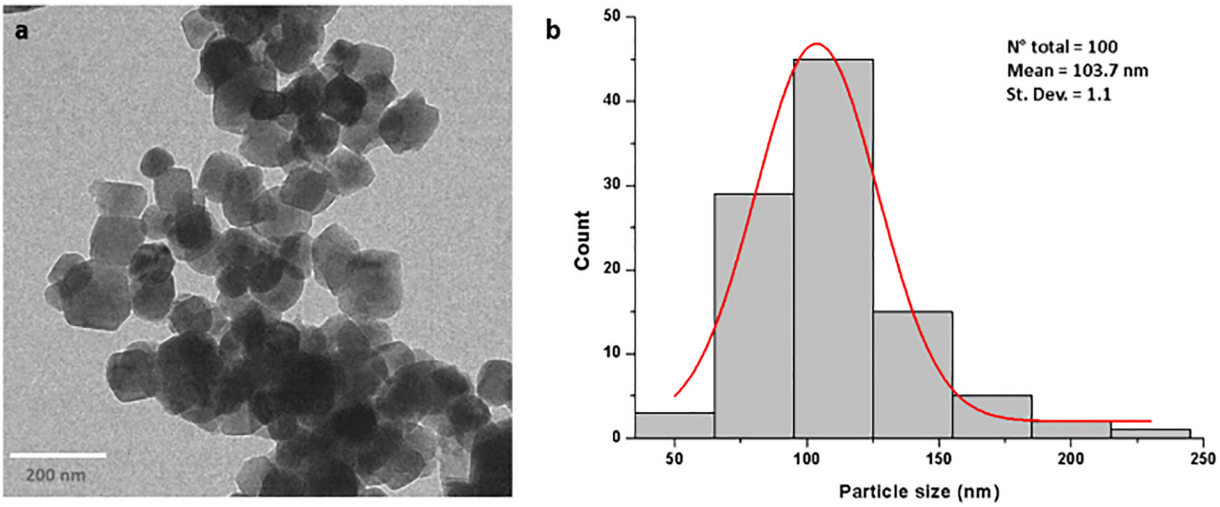

Fig. 2 TEM image of melanin–$CaCO_3$ NPs (a) and particle size distribution (b) obtained from the statistical analysis carried out after a random sampling of the nanoparticles.

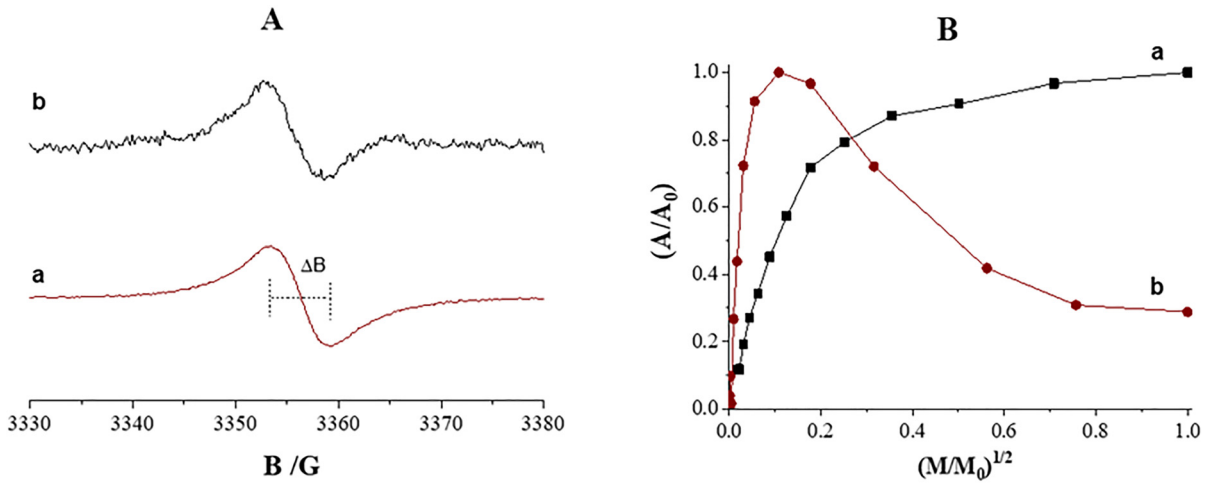

Fig. 3 (A) Normalized EPR spectra and (B) power saturation curve of the melanin pigment contained in synthetized melanin–$CaCO_3$ NPs (a) and DHICA-melanin (b) obtained from conventional oxidative polymerization in the absence of any inorganic matrix that can be considered as the reference.

spectroscopy. The absorption spectrum (Fig. S4) exhibits a characteristic broadband profile with a monotonic increase towards the UV region, culminating in a maximum intensity around 300 nm. This profile is typical of melanin-like pigments and confirms the successful functionalization of the $CaCO_3$ matrix. Importantly, this strong absorption in the UV range is a critical functional feature for the proposed application: it enables the nanoparticles to effectively act as 'optical shields' that filter high-energy radiation, thereby reducing the photo-oxidative burden on cells during the irradiation experiments described in Section 3.2.1. The close agreement of both the *g*-factor and ΔB values strongly supports the successful formation of melanin on the $CaCO_3$ NPs. Moreover, the spin density was estimated to be equal to 1.87×10^{17} spins g^{-1}, confirming the presence of melanin's radical centers and reflecting the total radical concentration per gram of nanostructured material, consistent with previously reported systems.[28,50,51] Finally, thermogravimetric analysis (TGA) provided a quantitative estimate of the melanin associated with $CaCO_3$ NPs, revealing a content of approximately 1%, as indicated by the weight loss (Fig. S5), thus confirming the low pigment loading in the hybrid melanin–$CaCO_3$ NPs. On the other hand, FTIR/ATR indicates similarities between the spectra of uncoated and melanin-coated $CaCO_3$ NPs (Fig. S6), which might be due to the fact that the main functional group of melanin is exposed in the same region of interest as $CaCO_3$'s ones, indirectly confirming that the coated sample is composed of a very low amount of pigment. All these findings clearly indicate that the inorganic $CaCO_3$ matrix facilitated the oxidative polymerization of the DHICA precursor into melanin.

3.2 Biological assays

3.2.1 NP–cell interaction. Human exposure to nanomaterials and nanoparticles is increasing rapidly, but their effects on human health are still largely unknown. Interestingly, our previous studies demonstrated an efficient cellular uptake of naked $CaCO_3$-NCs, amino-functionalized $CaCO_3$ nanocrystals, and bio-conjugated $CaCO_3$ nanocrystals by different cancer cell lines,[35,36,49] with a negligible cytotoxic effect.

In this work, before investigating the antioxidant and the cytoprotective effect of melanin–$CaCO_3$ NPs, at first, we evaluated the effect of exposure of HaCaT (human epidermal keratinocyte) and WS1 (fibroblast cell isolated from the skin) cell lines, to naked $CaCO_3$-NCs, NH_2-$CaCO_3$-NCs and melanin–$CaCO_3$ NPs. The use of HaCaT and WS1 is appropriate because these are the primary cell types found in human skin, the organ most directly affected by UV radiation and photo-oxidative stress. A very important aspect is the identification of the most relevant dose for particle toxicity, so in this context, HaCaT (Fig. 4a) and WS1 (Fig. 4c) cells were exposed for 24 hours to different concentrations of NPs (from 1 up to 200 μg mL^{-1}). No cytotoxic effect was observed; then, having fixed the concentration of 100 μg mL^{-1}, a time-course was carried out up to 72 h, for both cell lines (Fig. 4b and d). At 72 hours, there is a slight decrease in cell viability, but it does not appear to be statistically significant.

Furthermore, cell proliferation was examined by measuring the DNA concentration where an increase indicates cell growth. While melanin–$CaCO_3$ NPs did not seem to influence the metabolic activity of HaCaT and WS1 cells (Fig. 4), it significantly increased cell proliferation (Fig. 5). The evaluation of cytotoxicity and proliferation demonstrated the harmlessness of $CaCO_3$-NCs and NH_2-$CaCO_3$-NCs in both selected cell lines

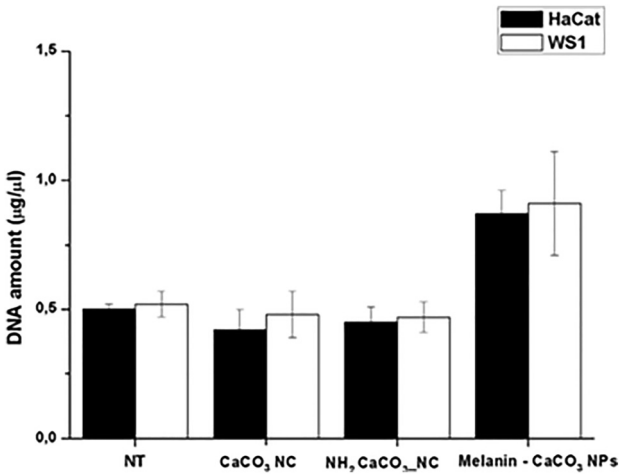

Fig. 5 Evaluation of cell proliferation with 10 μg mL^{-1} of naked $CaCO_3$ nanocrystals, amino-functionalized $CaCO_3$ nanocrystals, and melanin $CaCO_3$ cells (black bar) and WS1 cells (white bar). NT refers to untreated cells. Data represent means ± SD of three independent experiments.

in vitro at the selected concentrations. In contrast, although melanin–$CaCO_3$ NPs do not affect cell viability by reducing metabolic activity, the proliferation is considerably increased. Bare $CaCO_3$-NCs were employed as direct control because free DHICA-melanin was not readily obtainable in a form directly comparable to that produced on $CaCO_3$ nanoparticles. Indeed, DHICA-melanin functions as an organic dopant within the carbonate scaffold, modulating surface chemistry and redox behavior, thereby enabling a meaningful assessment of the hybrid material's biological effects.[52] To carry out the tests on photoprotective ability, the next culture conditions were chosen for being innocuous to both cell lines and, at the same time, containing the highest amount of melanin–$CaCO_3$ NPs.

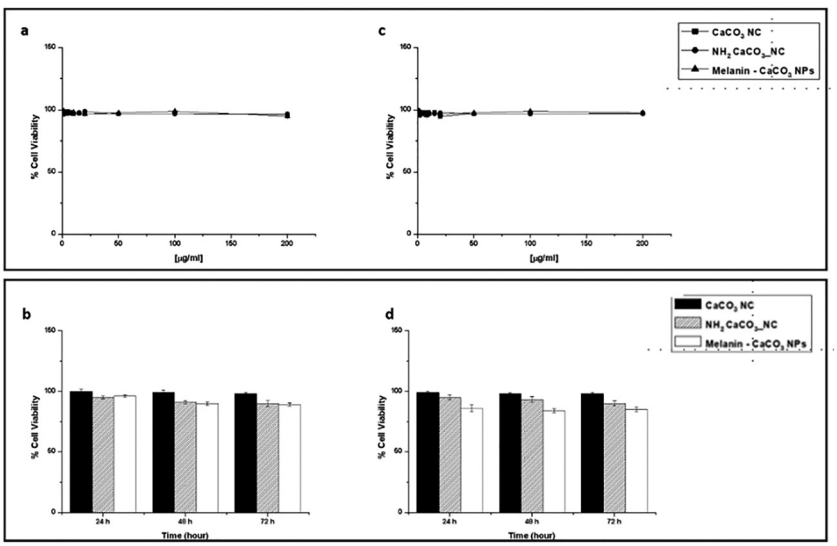

Fig. 4 Cell viability evaluation. Effect of $CaCO_3$-NCs, NH_2-$CaCO_3$-NCs, and melanin–$CaCO_3$ NPs on the viability of HaCaT (a) and WS1 (c) cells treated for 24 hours. The concentrations tested are in the range of 0 to 200 μM for each condition. Time-course up to 72 h of HaCaT (b) and WS1 (d) cells exposed to 100 μg mL^{-1} of $CaCO_3$ NC (black histogram), NH_2-$CaCO_3$-NCs (gray histogram), and melanin–$CaCO_3$ NPs (white histogram). Values represent mean ± SD and were obtained from five independent experiments.

As validated in our prior work,[35] $CaCO_3$ nanocrystals ensure safe long-term fate by dissolving in lysosomal acidity (~pH 5), preventing accumulation. In this study, cellular internalization, at different time points (3 h and 24 h), was evaluated by also confocal microscopy using melanin–$CaCO_3$ NPs conjugated with FITC. HaCaT and WS1 cells were incubated with 100 μg mL^{-1} of fluorescent melanin–$CaCO_3$ NPs, and the micrographs reported in Fig. 6 show how these NPs were internalized in the cells already only after 3 hours of exposure, as suggested by the green fluorescence reported in the central panel of the figure. The morphology of the nuclei shows that no alterations are observed even after long periods of incubation, confirming that there are no cytotoxic effects from the exposure of the cells to these NPs. To confirm internalization into cells, confocal Z-stacks were acquired (Fig. S3). To quantify the amount of internalized melanin–$CaCO_3$ NPs by cells, HaCaT and WS1 cells were subjected to incubation with melanin $CaCO_3$ NPs at a concentration of 10 μg mL^{-1} for a duration of 60 min. Subsequently, the complete cell lysates were carefully prepared. The ultraviolet-visible (UV-vis) spectra of lysates derived from both untreated and treated cells were recorded. Through this analysis, the extent of melanin internalized by the cells was estimated to be approximately 40% in HaCaT cells and 32% in WS1 cells. This estimation was based upon the absorbance measured at 330 nm in the lysates of the treated cells, with reference to the calibration curve established using pure melanin–$CaCO_3$ NPs (Fig. S4). The rate and the mechanism of internalization of $CaCO_3$ and NH_2-$CaCO_3$-NCs have been extensively investigated in different cancer cell line models, in our previous studies.[35,36]

3.2.2 Protective effect of melanin–$CaCO_3$ NPs against hydrogen peroxide-induced apoptosis. Melanin effectively scavenges a wide range of reactive species, including superoxide anion (O_2^-), hydrogen peroxide (H_2O_2), hydroxyl

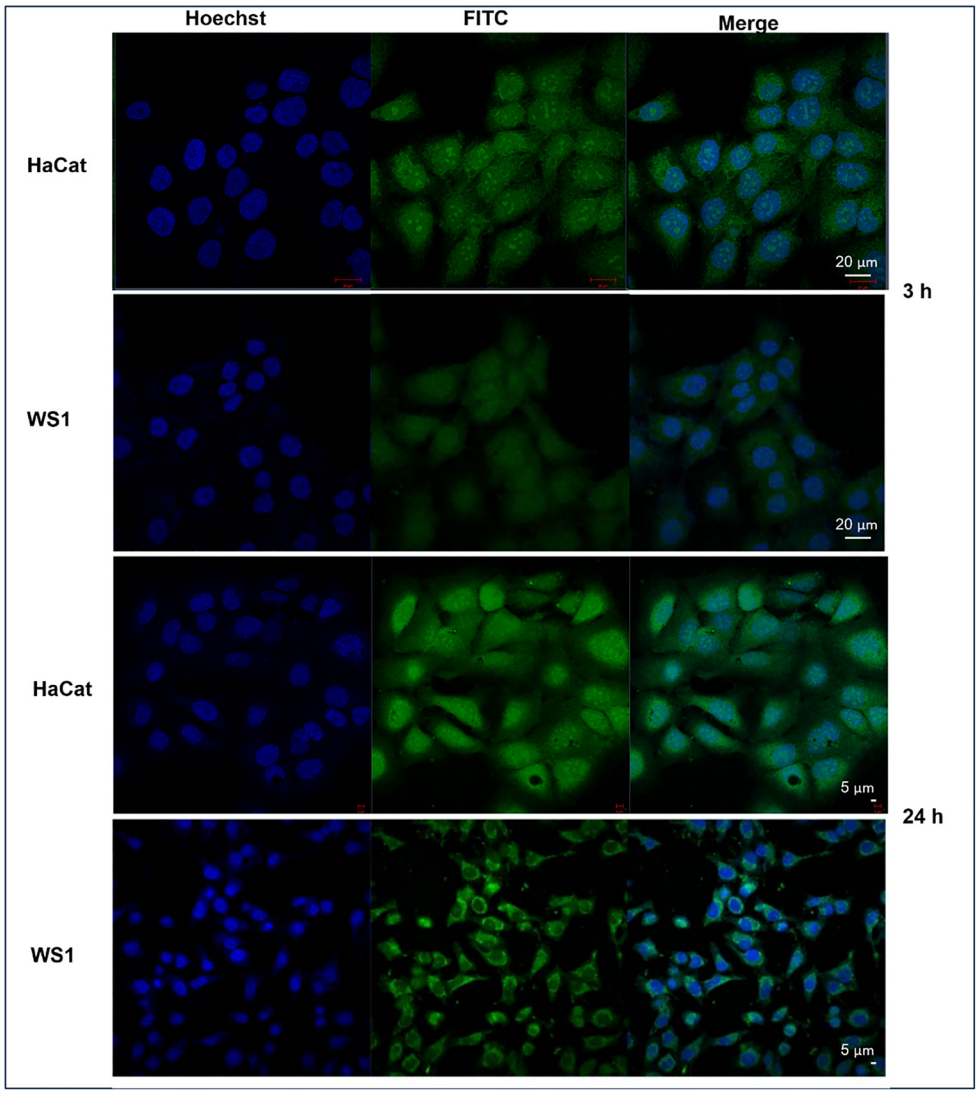

Fig. 6 Confocal images of HaCaT and WS1 cells treated with 100 μg mL^{-1} of melanin–$CaCO_3$ NPs conjugated with FITC. The green fluorescence signal is associated with NPs, and blue represents nuclei stained with Hoechst. The scale bar is indicated in each panel.

radicals (•OH), and nitric oxide (NO). Furthermore, it can also chelate metal ions (such as iron and copper), which are often involved in the generation of reactive species through Fenton reactions limiting ROS production.

The protective effect of melanin–$CaCO_3$ NPs against hydrogen peroxide-induced apoptosis was verified incubating HaCaT and WS1 cells for 24 h with NPs; then, the cells were treated with 1 mM H_2O_2 for 30 min. The apoptosis was assessed through FACS analysis staining the cells with annexin V. Fig. 7 demonstrates that all samples tested (naked $CaCO_3$ nanocrystals, amino-functionalized $CaCO_3$ nanocrystals, and melanin $CaCO_3$ NPs) were biocompatible both in HaCaT (Fig. 7a) and WS1 (Fig. 7b) cell lines. Hydrogen peroxide treatment induces a strong cell death and over 80% of cells were positive for annexin V in both cell lines. Instead, the preventive incubation of cells with melanin $CaCO_3$ NPs revealed a significative protective effect; indeed, the apoptotic cells were at most 32–35% in HaCaT and WS1 cells, respectively. This effect was due to the redox properties of dark eumelanin which plays a role in the protection from free radicals and oxidative insults.[51,53–55] This mechanistic interpretation is further supported by EPR measurements, which revealed the intrinsic radical character of melanin within the nanoparticles. Importantly, the paramagnetic character evidenced by EPR is directly linked to melanin's radical scavenging activity, as the presence of stable unpaired electrons provides redox-active centers capable of interacting with and neutralizing reactive species. These stable paramagnetic centers underpin its redox capacity, providing a direct link between the radical nature of melanin and the observed reduction of oxidative stress and apoptosis in treated cells. Furthermore, the protective role of melanin $CaCO_3$ NPs in the photoinduced oxidative stress against HaCaT and WS1 cell lines was assessed under UVA irradiation, chosen as a source of stress.[56] Ultraviolet irradiation may cause serious cellular and molecular tissue damage when living organisms are directly exposed without filtering.[57] This assay focused on UV blocking ability of our melanin $CaCO_3$ NPs against the damaging effects of UVA irradiation. A dose–response experiment was first performed incubating HaCaT and WS1 cells with increasing concentrations of naked $CaCO_3$-NCs, NH_2-$CaCO_3$-NCs, and melanin–$CaCO_3$ NPs (0.1–10 μg mL^{-1}) for 2 h prior to UVA irradiation treatment, and immediately after irradiation, ROS production was evaluated by the H_2DCFDA assay.

As shown in Fig. 8, at first, the HaCaT (a) and WS1 (b) cells were incubated at the maximum chosen concentration (10 μg mL^{-1}) of each sample to evaluate a possible ROS production related to nanomaterial exposure without UVA irradiation. In this case, DCF fluorescence did not show a significant increase, also in the presence of melanin–$CaCO_3$ NPs. Instead, ROS levels increased considerably on irradiated cells (Fig. 8c and d) under all tested conditions, but interestingly, only when cells were preincubated with melanin–$CaCO_3$ NPs prior to UVA exposure, ROS production was decreased in a dose dependent manner, reaching the levels observed in non-irradiated cells when the melanin–$CaCO_3$ NPs were tested already at 5 μg mL^{-1}. This evidence confirmed that the cytoprotective activity was exerted by the internalized melanin–$CaCO_3$ NPs, which acted inside the cells to preserve their integrity and not simply through a UV-shielding mechanism. Together with this peculiar behavior, these results appeared to be much more valuable considering the low content of melanin included in the final NPs which has already proven to be useful to confer a significant photoprotection ability to $CaCO_3$.[58–60] Several studies have shown that melanin nanoparticles, including those combined with $CaCO_3$, can exert protective effects within cells by scavenging ROS and reducing oxidative stress. This is especially significant because melanin's antioxidant properties are not restricted to UV protection but also include direct neutralization of free radicals and ROS in the cytoplasm,

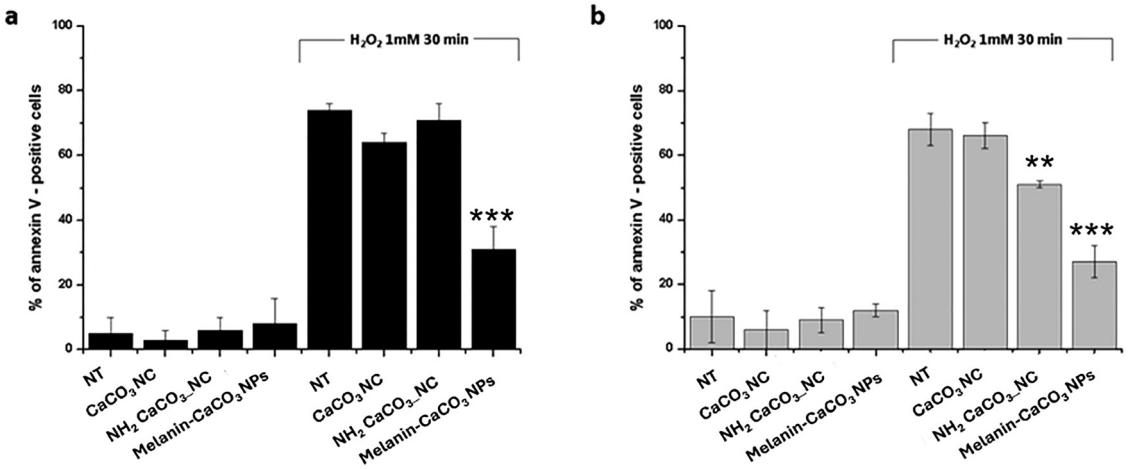

Fig. 7 Protective effect of naked $CaCO_3$ nanocrystals, amino-functionalized $CaCO_3$ nanocrystals, and melanin $CaCO_3$ NPs in two human cell lines. HaCaT cells (a) and WS1 cells (b) were treated with 1 mM H_2O_2 for 30 min after 24 h of incubation with melanin–$CaCO_3$ NPs followed by wash out of the particles. After 24 h of treatment, the cells were stained with annexin V, and the apoptosis was evaluated by FACS. NT: untreated with H_2O_2. Data are expressed as means ± standard error of the mean of three independent experiments. Statistical analysis was performed using two-way ANOVA followed by Sidak's multiple comparisons test. *p*-Values are indicated in the figure and represent the comparison between conditions (−H_2O_2 *vs.* +H_2O_2).

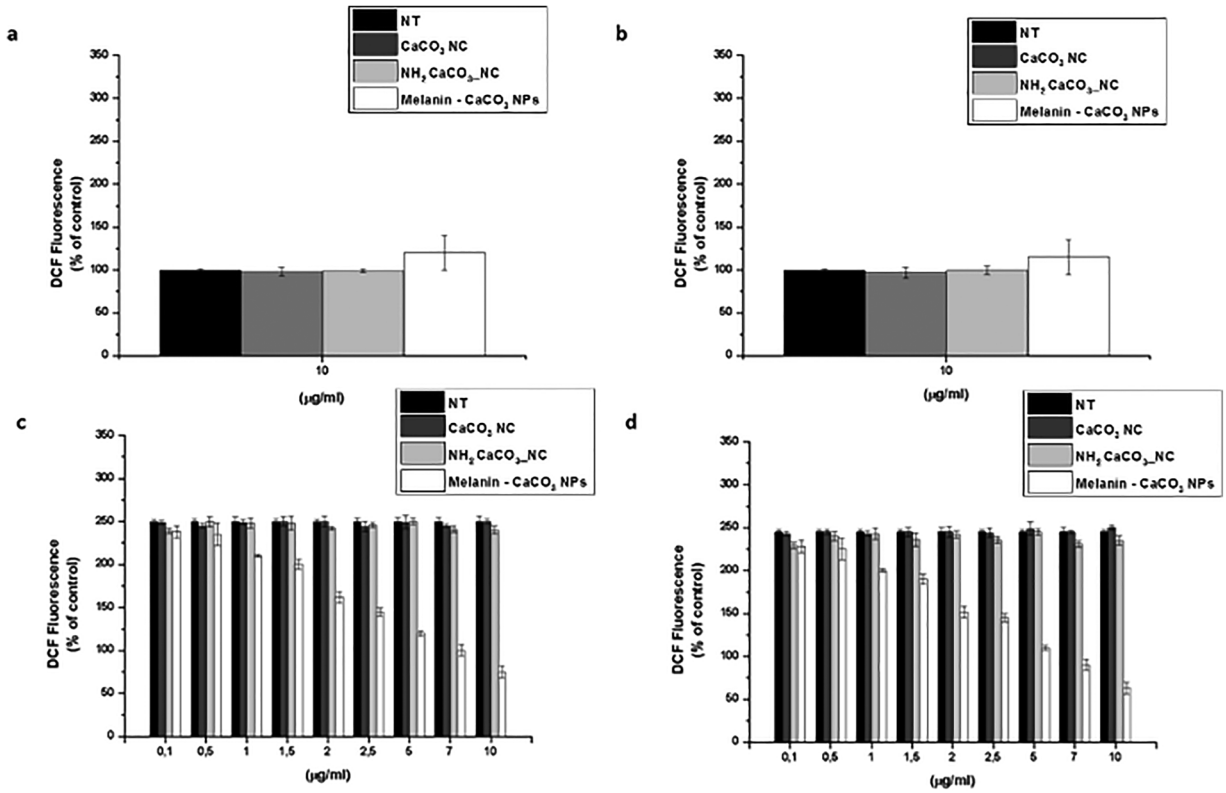

Fig. 8 Intracellular ROS levels by 2′,7′-dichlorodihydrofluorescein diacetate (H_2DCFDA) assay: antioxidant effects of $CaCO_3$-NCs (dark grey bars), NH_2-$CaCO_3$-NCs (light grey bars), and melanin–$CaCO_3$ NPs (white bars) on HaCaT cells (a) and WS1 cells (b) pre-incubated with 10 μg mL^{-1} of each sample for 2 h prior to 10 min of UVA irradiation (100 J cm^{-2}) . Black bars refer to untreated cells. Dose–response analysis: HaCaT cells (c) and WS1 cells (d) were pre-incubated with increasing concentrations of each sample for 2 h prior to 10 min of UVA irradiation (100 J cm^{-2}). Black bars refer to untreated cells. Values are expressed as % with respect to control (*i.e.* untreated) cells. Data shown are means ± SD of three independent experiments. Statistical analysis was performed using two-way ANOVA followed by Sidak's multiple comparison test. **** $p < 0.0001$ *vs.* the respective non-treated control (NT). Differences at 0.1 μg mL^{-1} were not statistically significant (ns).

mitochondria, and other cellular compartments. The choice of $CaCO_3$ as an inorganic support offers distinct advantages over traditional persistent materials like SiO_2, TiO_2, and CeO_2, particularly regarding intracellular fate and antioxidant safety. A comprehensive summary of the biological performance of the different nanoparticle systems, highlighting the superior properties of the melanin–hybrid design, is provided in Table 2. While metal-oxide supports such as TiO_2 can exhibit unintended pro-oxidant behaviour under UV exposure or cause 'dark toxicity' through mitochondrial interference, $CaCO_3$ is metabolically inert and undergoes pH-dependent biodegradation within acidic endo-lysosomal compartments. This ensures that the nanoparticles do not accumulate permanently within the cell, instead decompose into essential calcium ions that are safely integrated into cellular homeostasis. From a mechanistic standpoint, the $CaCO_3$ matrix facilitates a superior antioxidant performance by providing a high-surface-area, biocompatible scaffold that maximizes the accessibility of melanin's paramagnetic centers for ROS scavenging, avoiding the environmental fouling or surface-masking effects often observed with more chemically rigid inorganic cores. Furthermore, as reported in the literature, the size of our nanoparticles plays a crucial role in their antioxidant activity.[61,62] Recently, Carmignani *et al.* synthesized a series of melanin-mimic nanoparticles with sizes ranging from 150 to 960 nm and found that the scavenging efficiency was highest for the smallest nanoparticles.[63] Gianneschi and coworkers synthesized melanin-like NPs by simple polymerization of dopamine in an alkaline environment. They

Table 2 Summary of the comparative biological performance, including cell viability, proliferation, ROS scavenging efficiency, and cytoprotective activity of $CaCO_3$-NCs, NH_2-$CaCO_3$-NCs, and melanin–$CaCO_3$ NPs

Sample	Cell viability (up to 200 μg mL^{-1})	Cell proliferation	ROS scavenging efficiency	Cytoprotection (H_2O_2-induced apoptosis)
$CaCO_3$ NC	High (>95% – biocompatible)	Baseline	Negligible	None
NH_2-$CaCO_3$NC	High (>95% – biocompatible)	Baseline	Negligible	None
Melanin–$CaCO_3$ NPs	High (>95% – biocompatible)	Significantly increased	Very high (~50% reduction at 5 μg mL^{-1})	Significant (apoptosis reduced by ~60%)

reported the ROS-scavenging properties of these nanoparticles in human epidermal keratinocytes (HEKa).[64] All these studies underscored the critical relationship between the size and structural organization of melanin-like nanoparticles and their antioxidant efficacy, which could be presumably driven by the differential exposure and accessibility of specific chemical functional groups integral to radical scavenging mechanisms.

4. Conclusions

Oxidative stress occurs when there is an imbalance between the generation and accumulation of ROS in cells and tissues and the ability of the biological system to eliminate these reactive substances. The accumulation of oxidative damage can impair cellular function leading to DNA mutations or can trigger inflammatory responses exacerbating tissue damage and increasing cancer risk. Furthermore, chronic oxidative stress is associated with aging and the development of age-related diseases. The body employs antioxidants (*e.g.*, vitamin C, vitamin E, and glutathione) to neutralize ROS and minimize damage. Melanin nanoparticles have gained attention for their potential cytoprotective action, particularly in counteracting oxidative stress by absorbing UV radiation and scavenging ROS.[51,65,66]

This paper presents the synthesis of melanin–$CaCO_3$ NPs according to the *in situ* polymerization of DHICA on amino-functionalized $CaCO_3$ nanoparticles. The proposed strategy of using APTES-functionalized $CaCO_3$ nanoparticles ensures the colloidal stability of melanin-based nanosystems and the success of the polymerization process also favored by the alkaline conditions. The basic pH, promoting the oxidative polymerization of DHICA onto $CaCO_3$ nanoparticles, plays a crucial role in facilitating the conversion of DHICA into a stable polymeric structure, which is essential for the formation of melanin-like nanoparticles with enhanced stability and ROS-scavenging ability.

The produced NPs show a round shape morphology with a good biocompatibility and a high rate of cell internalization, important features for dermo-cosmetic applications.[67] The findings demonstrate that the melanin–$CaCO_3$ NPs are biocompatible, internalized by skin cells, and effectively protect them from oxidative stress induced by H_2O_2 and UVA irradiation. Indeed, these NPs protect immortalized human keratinocytes (HaCat) and fibroblasts (WS1) from damage caused by oxidative stress, as proved by the significantly reduction of stress parameters including ROS. Therefore, the protective action of melanin–$CaCO_3$ nanoparticles extends to intracellular mechanisms of oxidative stress mitigation, not just UV protection. The mechanism of antioxidant activity relies on the melanin's chemical structure, because it contains multiple phenolic groups and heteroatoms (such as nitrogen), which allow it to interact with and neutralize reactive molecules by scavenging free radicals and stabilizing cellular membranes. Also, these processes can help to protect cells from oxidative damage to lipids, proteins, and DNA.

The findings presented here provide new opportunities for the design of innovative hybrid nanoparticles with cytoprotective activity for nanomedicine applications. These nanoparticles offer a promising avenue for combating oxidative stress through their potent antioxidant activity and ability to protect cellular structures and modulate inflammatory responses. Their potential applications in therapeutic settings—particularly for neuroprotection, drug delivery, and overall cytoprotection—make them a subject of active further research in the fields of nanomedicine and biochemistry. However, further studies will need to include *in vivo* experiments, assess inflammatory markers, and evaluate long-term toxicity. These will be critical to fully determine the translational potential before any clinical application can be considered. On the other hand, advances in the precise tuning of nanostructures—from core–shell to cloud-type architectures—can further enhance their functional performance, as highlighted in the study.[30]

Author contributions

Vitiello G. and Vergaro V. wrote the manuscript, realized data analysis and prepared figures; Baldassarre F. contributed to physical–chemical and morphological characterization of nanoparticles. Pezzella A., Luciani G., Ciccarella G. and Boncristiani C. contributed to the revision of the manuscript; Vergaro V. coordinated the study and revised the manuscript. All authors read and approved the final manuscript. The manuscript was written through contributions of all authors. All authors have given approval to the final version of the manuscript.

Conflicts of interest

The authors declare that they have no known competing financial interests or personal relationships that could have appeared to influence the work reported in this paper.

Data availability

The authors confirm that all the supporting data and the findings of this study are included in the article and the attached supplementary information (SI). The supplementary materials include the following additional data concerning the (1) $CaCO_3$ nanoparticles characterization obtained by Transmission Electron Microscopy; (2) the stability characterization of nanoparticles performed by zeta potential measurements; (3) confocal micrographs: orthogonal projection image to confirm the internalization of nanoparticles; and (4) the quantification of internalized melanin–$CaCO_3$ nanoparticles performed by recording the UV-vis spectra; (5) TG and DTA curves of bare $CaCO_3$ NC and melanin–$CaCO_3$ NPs; (6) FTIR spectra of bare $CaCO_3$ and melanin–$CaCO_3$ NPs. See DOI: https://doi.org/10.1039/d5ma01417d.

Acknowledgements

We acknowledge financial support under the National Recovery and Resilience Plan (NRRP), Mission 4, Component 2, Investment 1.1, Call for tender no. 104 published on 2.2.2022 by the Italian Ministry of University and Research (MUR), funded by the European Union – NextGenerationEU – Project Title MulticEllular spheRoids model for muLtiparametric blood–brain barrier Injury detectioN in microfluidics (MERLIN) – CUP B53D23018380006 by the Italian Ministry of Ministry of University and Research (MUR). The authors also thank the Department of Chemical Science of University of Naples Federico II for awarding time for EPR measurements. Regione Puglia within ''Tecnopolo per la medicina di precisione'' (TecnoMed Puglia): DGR n.2117 del 21/11/2018, CUP: B84I180 0 0540 0 02.

References

1 Y. A. Hajam, R. Rani, S. Y. Ganie, T. A. Sheikh, D. Javaid, S. S. Qadri, S. Pramodh, A. Alsulimani, M. F. Alkhanani, S. Harakeh, A. Hussain, S. Haque and M. S. Reshi, *Cells*, 2022, **11**, 552.
2 D. Rotariu, E. E. Babes, D. M. Tit, M. Moisi, C. Bustea, M. Stoicescu, A. F. Radu, C. M. Vesa, T. Behl, A. F. Bungau and S. G. Bungau, *Biomed. Pharmacother.*, 2022, **152**, 113238.
3 A. Laurent, C. Nicco, C. Chéreau, C. Goulvestre, J. Alexandre, A. Alves, E. Lévy, F. Goldwasser, Y. Panis, O. Soubrane, B. Weill and F. Batteux, Controlling Tumor Growth by Modulating Endogenous Production of Reactive Oxygen Species, *Cancer Res.*, 2005, **65**, 948–956.
4 B. Kalyanaraman, G. Cheng and M. Hardy, *Redox Biol.*, 2024, **71**, 103092.
5 S. Di Meo, T. T. Reed, P. Venditti and V. M. Victor, *Oxid. Med. Cell. Longev.*, 2016, **2016**, 1245049.
6 N. Zarkovic, *Cells*, 2020, **9**, 767.
7 K. Jomova, R. Raptova, S. Y. Alomar, S. H. Alwasel, E. Nepovimova, K. Kuca and M. Valko, *Arch. Toxicol.*, 2023, **97**, 2499–2574.
8 M. Lodovici and E. Bigagli, *J. Toxicol.*, 2011, **2011**, 487074.
9 P. Irato and G. Santovito, *Antioxidants*, 2021, **10**, 579.
10 Y. Dai, Y. Guo, W. Tang, D. Chen, L. Xue, Y. Chen, Y. Guo, S. Wei, M. Wu, J. Dai and S. Wang, *J. Nanobiotechnol.*, 2024, **22**, 252.
11 F. Wei, W. Yang, H. Wang, S. Song, Y. Ji, Z. Chen, Y. Zhuang, J. Dai and H. Shen, *Biomater. Sci.*, 2025, **13**, 343–363.
12 F. Fragou, A. Theofanous, Y. Deligiannakis and M. Louloudi, *Micromachines*, 2023, **14**, 383.
13 P. Wen, A. Dirisala, H. Guo, X. Liu, S. Kobayashi, H. Kinoh, T. Anada, M. Tanaka, K. Kataoka and J. Li, *J. Controlled Release*, 2025, **382**, 113683.
14 A. R. Hegde, M. U. Kunder, M. Narayanaswamy, S. Murugesan, S. C. Furtado, B. B. Veerabhadraiah and B. Srinivasan, *Environ. Sci. Pollut. Res. Int.*, 2024, **31**, 38061–38082.
15 M. Burkard, A. Betz, K. Schirmer and A. Zupanic, *Environ. Sci. Technol.*, 2020, **54**, 335–344.
16 L. Guo, W. Li, Z. Gu, L. Wang, L. Guo, S. Ma, C. Li, J. Sun, B. Han and J. Chang, *Int. J. Mol. Sci.*, 2023, **24**, 4360.
17 J. Y. Lin and D. E. Fisher, *Nature*, 2007, **445**, 843–850.
18 M. Brenner and V. J. Hearing, *Photochem. Photobiol.*, 2008, **84**, 539–549.
19 M. Jinek, K. Chylinski, I. Fonfara, M. Hauer, J. A. Doudna and E. Charpentier, A programmable dual RNA-guided DNA endonuclease in adaptive bacterial immunity One-Sentence Summary, *Science*, 2012, **337**, 816–821.
20 S. D. Seelam, D. Agsar, S. K. Halmuthur M., P. Reddy Shetty, S. Vemireddy, K. M. Reddy, M. K. Umesh and C. H. Rajitha, *J. Photochem. Photobiol., B*, 2021, **216**, 112126.
21 Z. Lin, L. Liu, W. Wang, L. Jia, Y. Shen, X. Zhang, D. Ge, W. Shi and Y. Sun, *Biomater. Sci.*, 2021, **9**, 5951–5964.
22 S. Zhang, Q. Ou, P. Xin, Q. Yuan, Y. Wang and J. Wu, *Biomater. Sci.*, 2019, **7**, 4230–4236.
23 T. Rahmani Eliato, J. T. Smith, Z. Tian, E. S. Kim, W. Hwang, C. P. Andam and Y. J. Kim, *J. Mater. Chem. B*, 2021, **9**, 1536–1545.
24 J. J. Oh, J. Y. Kim, S. H. Son, W. J. Jung, D. H. Kim, J. W. Seo and G. H. Kim, *RSC Adv.*, 2021, **11**, 19682–19689.
25 W. Cheng, X. Zeng, H. Chen, Z. Li, W. Zeng, L. Mei and Y. Zhao, *ACS Nano*, 2019, **13**, 8537–8565.
26 G. Pota, A. Zanfardino, M. Di Napoli, D. Cavasso, M. Varcamonti, G. D'Errico, A. Pezzella, G. Luciani and G. Vitiello, *Colloids Surf., B*, 2021, **202**, 111671.
27 B. Silvestri, G. Vitiello, G. Luciani, V. Calcagno, A. Costantini, M. Gallo, S. Parisi, S. Paladino, M. Iacomino, G. D'Errico, M. F. Caso, A. Pezzella and M. D'Ischia, *ACS Appl. Mater. Interfaces*, 2017, **9**, 37615–37622.
28 G. Pota, B. Silvestri, G. Vitiello, N. Gallucci, R. Di Girolamo, S. Scialla, M. G. Raucci, L. Ambrosio, M. Di Napoli, A. Zanfardino, M. Varcamonti, A. Pezzella and G. Luciani, *Biomater. Adv.*, 2023, **153**, 213558.
29 F. Furlani, G. Pota, A. Rossi, G. Luciani, E. Campodoni, F. Mocerino, G. D'Errico, A. Pezzella, S. Panseri, G. Vitiello and M. Sandri, *Colloids Surf., B*, 2024, **235**, 113756.
30 G. Pota, G. Vitiello, V. Venezia, F. Della Sala, A. Borzacchiello, A. Costantini, L. Paduano, L. P. Cavalcanti, F. Tescione, B. Silvestri and G. Luciani, *Polymers*, 2022, **14**, 3568.
31 P. Durgadevi, K. Girigoswami and A. Girigoswami, *Physics*, 2025, **7**, 28.
32 P. Pallavi, K. Girigoswami, K. Harini, P. Gowtham, A. Thirumalai and A. Girigoswami, *Naunyn. Schmiedebergs. Arch. Pharmacol.*, 2025, **398**, 867–880.
33 P. Pallavi, K. Harini, S. Crowder, D. Ghosh, P. Gowtham, K. Girigoswami and A. Girigoswami, *Appl. Biochem. Biotechnol.*, 2023, **195**, 6979–6993.
34 Y. Zhao, Y. Bian, X. Xiao, B. Liu, B. Ding, Z. Cheng, P. Ma and J. Lin, *Small*, 2022, **18**, 2204047.
35 V. Vergaro, E. Carata, F. Baldassarre, E. Panzarini, L. Dini, C. Carlucci, S. Leporatti, B. F. Scremin, D. Altamura, C. Giannini, F. P. Fanizzi and G. Ciccarella, *Adv. Powder Technol.*, 2017, **28**, 2445–2455.
36 V. Vergaro, I. Pisano, R. Grisorio, F. Baldassarre, R. Mallamaci, A. Santoro, G. P. Suranna, P. Papadia, F. P. Fanizzi and G. Ciccarella, *Materials*, 2019, **12**, 1481.

37 D. Vecchione, A. M. Grimaldi, E. Forte, P. Bevilacqua, P. A. Netti and E. Torino, *Sci. Rep.*, 2017, **7**, 45121.
38 U. Freudenberg, Y. Liang, K. L. Kiick and C. Werner, *Adv. Mater.*, 2016, **28**, 8861–8891.
39 M. D'Ischia, K. Wakamatsu, A. Napolitano, S. Briganti, J. C. Garcia-Borron, D. Kovacs, P. Meredith, A. Pezzella, M. Picardo, T. Sarna, J. D. Simon and S. Ito, *Pigm. Cell Melanoma Res.*, 2013, **26**, 616–633.
40 V. Vergaro, P. Papadia, S. Leporatti, S. A. De Pascali, F. P. Fanizzi and G. Ciccarella, *J. Inorg. Biochem.*, 2015, **153**, 284–292.
41 E. Wondu, Z. C. Lule and J. Kim, *Polymers*, 2020, **12**, 747.
42 N. Chekina, D. Horák, P. Jendelová, M. Trchová, M. J. Beneš, M. Hrubý, V. Herynek, K. Turnovcová and E. Syková, *J. Mater. Chem.*, 2011, **21**, 7630–7639.
43 G. Vitiello, A. Pezzella, V. Calcagno, B. Silvestri, L. Raiola, G. D'Errico, A. Costantini, F. Branda and G. Luciani, *J. Phys. Chem. C*, 2016, **120**, 6262–6268.
44 D. Liberti, M. L. Alfieri, D. M. Monti, L. Panzella and A. Napolitano, *Antioxidants*, 2020, **9**, 270.
45 É. Velot, F. Ducrocq, L. Girardeau, A. Hehn, S. Piutti, C. Kahn, M. Linder, A. Bianchi and E. Arab-Tehrany, *Int. J. Mol. Sci.*, 2022, **23**, 12423.
46 A. Bianchi, É. Velot, H. Kempf, K. Elkhoury, L. Sanchez-Gonzalez, M. Linder, C. Kahn and E. Arab-Tehrany, *Int. J. Mol. Sci.*, 2020, **21**, 3436.
47 V. Vergaro, F. Baldassarre, F. De Castro, D. Migoni, M. M. Dell'Anna, P. Mastrorilli, F. P. Fanizzi and G. Ciccarella, *Bioinorg. Chem. Appl.*, 2022, **2022**, 9571217.
48 B. Silvestri, G. Vitiello, G. Luciani, V. Calcagno, A. Costantini, M. Gallo, S. Parisi, S. Paladino, M. Iacomino, G. D'Errico, M. F. Caso, A. Pezzella and M. d'Ischia, *ACS Appl. Mater. Interfaces*, 2017, **9**, 37615–37622.
49 V. Vergaro, M. Civallero, C. Citti, M. Cosenza, F. Baldassarre, G. Cannazza, S. Pozzi, S. Sacchi, F. P. Fanizzi and G. Ciccarella, *Cancers*, 2018, **10**, 31.
50 G. Pota, A. Puzone, E. Carrella, A. Pezzella, G. Luciani, G. D'Errico and G. Vitiello, *Appl. Surf. Sci.*, 2025, **686**, 162134.
51 L. Panzella, G. Gentile, G. D'Errico, N. F. Della Vecchia, M. E. Errico, A. Napolitano, C. Carfagna and M. D'Ischia, *Angew. Chem., Int. Ed.*, 2013, **52**, 12684–12687.
52 K. Urabe, P. Aroca, K. Tsukamoto, D. Mascagna, A. Palumbo, G. Prota and V. J. Hearing, *Biochim. Biophys. Acta*, 1994, **1221**, 272–278.
53 B.-L. L. Seagle, K. A. Rezai, Y. Kobori, E. M. Gasyna, K. A. Rezaei and J. R. Norris, *Proc. Natl. Acad. Sci. U. S. A.*, 2005, **102**, 8978–8983.
54 K. Y. Ju, Y. Lee, S. Lee, S. B. Park and J. K. Lee, *Biomacromolecules*, 2011, **12**, 625–632.
55 T. Sarna, *Photochem. Photobiol.*, 2023, **99**, 866–868.
56 R. M. Haywood, M. Lee and C. Linge, *J. Photochem. Photobiol., B*, 2006, **82**, 224–235.
57 R. Brem, M. Guven and P. Karran, *Free Radical Biol. Med.*, 2017, **107**, 101–109.
58 L. Guo, T. Wang, Z. Li, S. Wu, Y. Xu, Z. Yang, Y. Li, Z. Gu and X. Jiang, *Chem. Mater.*, 2023, **35**, 5420–5432.
59 Z. Dong, L. Feng, Y. Hao, M. Chen, M. Gao, Y. Chao, H. Zhao, W. Zhu, J. Liu, C. Liang, Q. Zhang and Z. Liu, *J. Am. Chem. Soc.*, 2018, **140**, 2165–2178.
60 X. Ru, Y. Guo, Z. Bai, X. Xie, X. Ma, L. Zhu, K. Wang, F. Wang, L. Yang and J. Lu, *Commun. Chem.*, 2019, **2**, 105.
61 A. Mavridi-Printezi, A. Menichetti, D. Mordini, R. Amorati and M. Montalti, *Antioxidants*, 2023, **12**, 863.
62 G. Zhong, X. Yang, X. Jiang, A. Kumar, H. Long, J. Xie, L. Zheng and J. Zhao, *Nanoscale*, 2019, **11**, 11605–11616.
63 A. Carmignani, M. Battaglini, E. Sinibaldi, A. Marino, V. Vighetto, V. Cauda and G. Ciofani, *ACS Appl. Nano Mater.*, 2022, **5**, 1702–1713.
64 Y. Huang, Y. Li, Z. Hu, X. Yue, M. T. Proetto, Y. Jones and N. C. Gianneschi, *ACS Cent. Sci.*, 2017, **3**, 564–569.
65 S. Jiang, X. M. Liu, X. Dai, Q. Zhou, T. C. Lei, F. Beermann, K. Wakamatsu and S. Z. Xu, *Free Radical Biol. Med.*, 2010, **48**, 1144–1151.
66 S. Ito, M. Kikuta, S. Koike, G. Szewczyk, M. Sarna, A. Zadlo, T. Sarna and K. Wakamatsu, *Pigm. Cell Melanoma Res.*, 2016, **29**, 340–351.
67 R. Micillo, M. Iacomino, M. Perfetti, L. Panzella, K. Koike, G. D'Errico, M. d'Ischia and A. Napolitano, *Pigm. Cell Melanoma Res.*, 2018, **31**, 475–483.